Mineralogy and geochemistry of El Dorado epithermal gold deposit, El Sauce district, central-northern Chile

J. Carrillo-Rosúa[1,2,3], **S. Morales-Ruano**[1], **D. Morata**[2], **A. J. Boyce**[3], **M. Belmar**[2], **A. E. Fallick**[3], and **P. Fenoll Hach-Alí**[1]

[1] Dpto. de Mineralogía y Petrología, and Instituto Andaluz de Ciencias de la Tierra, Universidad de Granada-CSIC, Granada, Spain
[2] Dpto. de Geología, Universidad de Chile, Santiago, Chile
[3] Isotope Geosciences Unit, SUERC, East Kilbride (Glasgow), Scotland, U.K.

Summary

The El Dorado Au-Cu deposit is located in an extensive intra-caldera zone of hydrothermal alteration affecting Upper Cretaceous andesites of the *Los Elquinos Formation* at La Serena ($\approx 29°47'$S Lat., $70°43'$W Long., Chile). Quartz-sulfide veins of economic potential are hosted by N25W and N20E fault structures associated with quartz-illite alteration (+supergene kaolinite). The main ore minerals in the deposit are pyrite, chalcopyrite ± fahlore (As/(As + Sb): 0.06–0.98), with electrum, sphalerite, galena, bournonite-seligmanite (As/(As + Sb): 0.21–0.31), marcasite, pyrrhotite being accessory phases. Electrum, with an Ag content between 32 and 37 at.%, occurs interstitial to pyrite aggregates or along pyrite fractures. Pyrite commonly exhibits chemical zonation with some zones up to 1.96 at.% As. Electron probe microanalyses of pyrite indicate that As-rich zones do not exhibit detectable Au values. Fluid inclusion microthermometry shows homogenization temperatures between 130 and 352 °C and salinities between 1.6 and 6.9 wt.% NaCl eq. Isotope data for quartz, ankerite and phyllosilicates and estimated temperatures show that δ^{18}O and δD for the hydrothermal fluids were between 3 and 10‰ and between −95 and −75‰, respectively. These results suggest the mineralizing fluids were a mixture of meteoric and magmatic waters. An epithermal intermediate-sulfidation model is proposed for the formation of the El Dorado deposit.

Introduction

Epithermal deposits constitute an important target for gold exploration since they contribute significantly to the world gold production. These deposits frequently

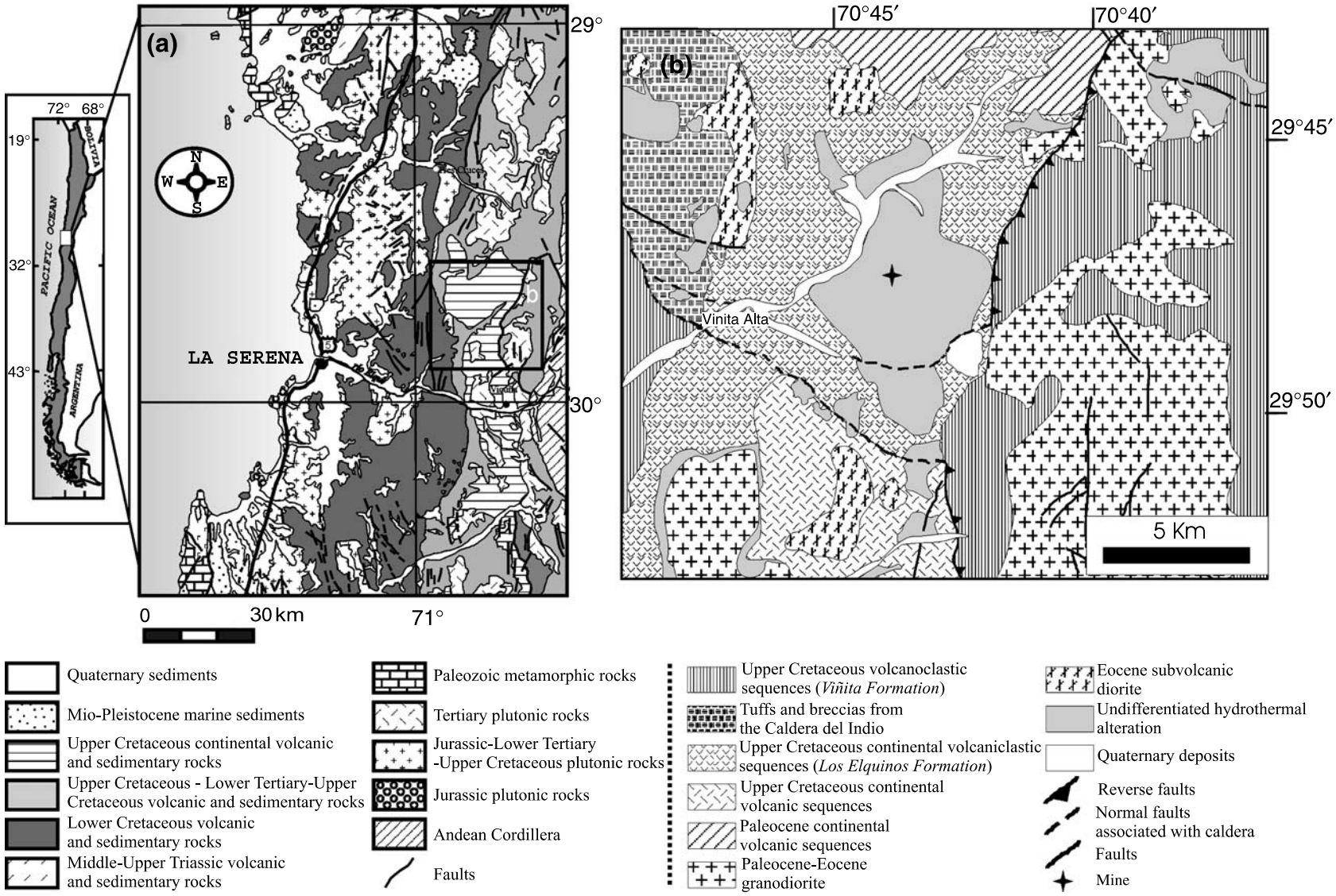

Fig. 1. (**a**) Geological map (modified according to *Emparan* and *Pineda* (1999, 2000a, 2007) and simplified from the *SERNAGEOMIN* (2002) geological map showing the location of the studied area. (**b**) Detailed geological map of the El Sauce District and location of the El Dorado gold-bearing epithermal deposit (simplified from *Emparan* and *Pineda*, 1999)

crop out in active (continental or island arc) margins and are usually, although with significant exceptions, younger than Paleocene. Au, Cu and Ag are the most common economic metals, and Pb-Zn are locally important. On the basis of ore and gangue minerals, alteration mineralogy, textures and characteristics of hydrothermal fluids, these deposits have been classically grouped in high and low-sulfidation types (e.g., *Hedenquist* et al., 2000; *Simmons* et al., 2005). Epithermal deposits are common in the Chilean-Andes, with high-sulfidation epithermal deposits characteristic from the Miocene-Pleistocene, and low-sulfidation from the Mesozoic to Paleogene (e.g., *Camus*, 1990; *Sillitoe*, 1991). It is noteworthy that deposits from the Miocene-Pleistocene represent higher reserves of gold and copper than older deposits (e.g., *Camus*, 1990).

This paper presents the results of the first study of the mineralogy and mineral chemistry (XRD, SEM and EMPA), fluid inclusion microthermometry and stable isotope geochemistry of the El Dorado Cu-Au deposit. The deposit occurs within pervasively hydrothermally altered volcanic rocks of Upper Cretaceous age in the Precordillera of central-north Chile, at $\approx 29°47'$ Lat. S $70°43'$W Long. (Fig. 1). We discuss the genesis of this deposit within the Late Cretaceous – Paleogene geodynamic evolution of this segment of the Coastal Range and Precordillera, and we present a classification of the deposit. Our study focuses on the ore mineralogy and mineral chemistry, with emphasis on precious metal (Au and Ag) and related minerals (i.e., pyrite contents and their occurrence). This is providing the foundation for the further geochemical and mineralogical investigations.

Geological setting

In the Coastal Range and Precordillera of the La Serena area, along the Elqui Valley, a complete Cretaceous to Tertiary volcano-sedimentary sequence is present (Fig. 1a). The Lower Cretaceous rocks are included in the *Arqueros* and *Quebrada Marquesa Formations*, while the Upper Cretaceous volcaniclastic rocks are represented by the upper part of *Viñita* and *Los Elquinos Formations* (*Aguirre* and *Egert*, 1965; *Pineda* and *Emparan*, 1997; *Emparan* and *Pineda*, 1999). A change in the depositional conditions from shallow-water marine basins in the Lower Cretaceous to continental in the Upper Cretaceous sedimentary sequences has been proposed by *Pineda* and *Emparan* (1997).

Only limited geochronological data are available for basaltic lavas belonging to the *Viñita Formation*; a K-Ar age of 82 ± 3 Ma (whole-rock, *Pineda* and *Emparan*, 1997) must be interpreted as a minimum age due to alteration, rather than the age of lava extrusion (Fig. 1b), while zircon U-Pb ages of 84.8 ± 0.3 Ma and 84.6 ± 0.2 Ma were obtained from stratigraphically higher rhyodacites of this formation (*Emparan* and *Pineda*, 2000b). A U-Pb zircon age of 70 ± 3 Ma has been obtained by *Emparan* and *Pineda* (2000b) for the *Los Elquinos Formation*, in rhyodacites from the upper levels of this formation. Consequently, Late Cretaceous volcanism in the area may range from ≈90–95 Ma (assumed age for the extrusion of lower basaltic lavas of the *Viñita Formation*, *Morata* et al., 2003) up to 70–65 Ma.

Based on stratigraphic and tectonic evidence (*Pineda* and *Emparan*, 1997; *Emparan* and *Pineda*, 2000b) as well as geochemical studies of volcanism

(*Morata* and *Aguirre*, 2003; *Morata* et al., 2003), an extensional regime has been proposed during the Early Cretaceous. The geochemistry and primary isotopic signature of the Late Cretaceous basic lavas (*Morata* et al., 2003), suggest more intense extensional conditions during this time compared to the Early Cretaceous. The extensional volcanism cycle ended with regional caldera collapse at ca. 85 Ma (*Pineda* and *Emparan*, 1997), followed by a progressive geodynamic change to compressional regime, as evidenced by the development of asymmetrical anticlines during the Eocene (*Pineda* and *Emparan*, 1997).

Paleocene-Eocene epizonal granodioritic intrusions were emplaced into the Late Cretaceous formations, developing in some cases intense hydrothermal alteration zones around these intrusions (Fig. 1b). The El Dorado prospect is one of several ore deposits within the El Sauce District (also known as El Guanaco area, *Jorquera*, 2005), and is located around 25 km NE of Viñita village (UTM coordinates 332680 E; 6703500 N, Fig. 1). The El Dorado deposit is placed in the central part of the El Sauce District, a strongly hydrothermally altered intracaldera area (ca. 30 km^2 wide) with Cu-Au-Ag mineralization mostly hosted

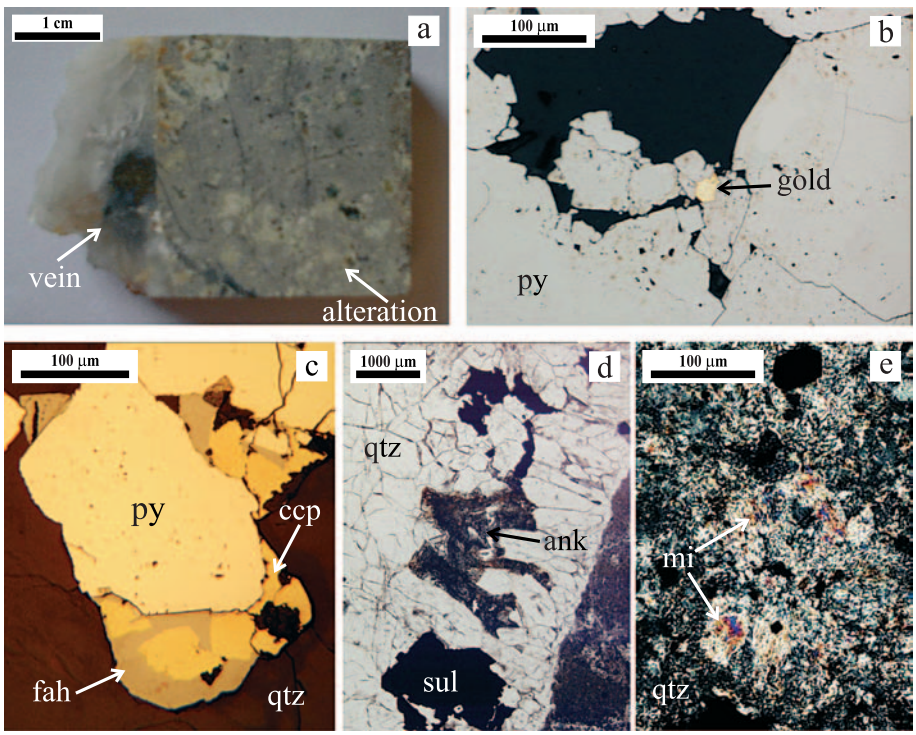

Fig. 2. Photograph (**a**) and photomicrographs (**b**–**e**) of the El Dorado mineralization and related hydrothermal alteration. (**a**) Hand specimen of a quartz vein with sulfides crosscutting hydrothermally altered dacite-andesite from the *Los Elquinos Formation*. (**b**) Interstitial gold grain in coarse pyrite (*py*) aggregate. (**c**) Typical association of chalcopyrite (*ccp*), fahlore (*fah*) and pyrite (*py*) crystals. (**d**) Sulfides (*sul*) and ankerite (*ank*) interstitial to quartz (*qtz*) crystals within a mineralized vein. (**e**) Intergrowth of quartz (*qtz*) and mica (*mi*) crystals within the vein

in Upper Cretaceous-Paleocene volcanic and volcaniclastic rocks intruded by Paleocene-Eocene epizonal and hypabysal granitoids (*Jorquera*, 2005). The El Dorado deposit was exploited in 1936 when 4.72 kg of Au were produced. Later, during 1981 the deposit was re-worked, with Au up to 12 g/t (*Jorquera*, 2005). The El Dorado gold mineralization is hosted by steeply dipping veins and veinlets of quartz with sulfides, crosscutting dacites, andesites and andesitic breccias of the *Los Elquinos Formation* (Fig. 1b), along two well defined (N25W and N20E) structural directions (*Jorquera*, 2005). Mineralized veins extend along several hundred of metres, with 0.4–1.5 m thickness and up to 150 m deep (*Jorquera*, 2005). The volcanic rocks are affected by pervasive hydrothermal alteration which is thought to be closely related to mineralization processes (Fig. 2a).

Analytical techniques

Representative samples were collected to determine the mineralogy and paragenetic relationships among the ore minerals in the veins and the hydrothermally altered host-rock. Fluid inclusion and stable isotope chemistry were studied to characterize the mineralizing fluids involved in the genesis of the ore deposit.

The mineralogy of the ore and alteration minerals, and their mineral chemistry, were studied using a PHILLIPS PW 1710® X-ray diffractometer at the Department of Mineralogy and Petrology, University of Granada, reflected and transmitted light microscopy, scanning electron microscopy and electron probe micro analysis (SEM: LEO GEMINI 1530® field emission scanning electron microscope, EPMA: CAMECA SX50® electron microprobe; both instruments are located at the ''Centro de Instrumentación Científica'', University of Granada). Natural and synthetic certified standards were used to calibrate WDS quantitative analysis. The operating conditions were 20–30 kV accelerating potential, 20–30 nA beam current and acquisition time between 60 and 300 s for X-ray peak and background. The acquired X-ray intensities were corrected for atomic number, mass-absorption and secondary fluorescence effects using the CAMECA-PAP version of the *Pouchou* and *Pichoir* (1984) procedure. X-ray mapping was performed under 30 kV accelerating potential, 200 nA beam current, 2 μm scan distance, and 150 ms X-ray peak acquisition time per point as analytical conditions.

Microthermometric measurements were performed on doubly-polished thin-sections about 100 μm thick using a Linkam® THMSG 600 freezing-heating stage, a TMS93 temperature control system, and LNP2 freezing control system in the Fluid Inclusion Laboratory, Department of Mineralogy and Petrology, University of Granada. The fluid inclusion stage was calibrated with Merck® inorganic standards in the range from −95 to 419 °C. The data are reproducible to ±0.5 °C for the freezing runs and ±5 °C for the heating runs. The fluid inclusions were analyzed following the procedures described by *Shepherd* et al. (1985). Values of salinity were calculated using the melting temperature of the last ice crystal (*Potter* et al., 1978).

Sulfur for isotope analyses from sulfide samples was extracted following *Robinson* and *Kusakabe* (1975). Liberated gases were analysed on a VG Isotech

SIRA II® mass spectrometer. Data are reported in $\delta^{34}S$ notation as per mil (‰) variations from the Vienna Cañon Diablo Troilite (V-CDT) standard.

Oxygen isotopes in silicate samples were analyzed using a laser fluorination procedure, involving total sample reaction with excess ClF_3 using a CO_2 laser as a heat source (in excess of 1500 °C; following *Sharp*, 1990). The extracted O_2 was then converted to CO_2 by reaction with hot graphite, then analysed on-line by a VG PRISM III® spectrometer. Reproducibility is better than ± 0.3‰ (1σ). Results are reported in standard notation ($\delta^{18}O$) as per mil (‰) deviations from the Standard Mean Ocean Water (V-SMOW) standard. Samples were analysed for hydrogen isotopes using standard techniques (*Donnelly* et al., 2001). Thus, H_2O was extracted from degassed overnight samples by radiofrequency induction heating and then reduced to H_2 in a chromium furnace. The gas was subsequently analysed on a VG 602D® mass spectrometer. Replicate analyses of water standards (international standards V-SMOW and GISP, and internal standard Lt Std) gave a reproducibility of ± 2‰. Replicate analyses of international mineral standard NBS-30 (biotite) also gave reproducibility around ± 2‰. CO_2 for isotope analyses was quantitatively released from the ankerite samples by the standard procedure of overnight reaction *in vacuo* with 100% phosphoric acid at 100 °C. Gases thus produced were analysed on a VG SIRA 10® mass spectrometer. Analytical raw data were corrected using standard procedures (*Craig*, 1957). Isotope data are reported in standard δ-notation as per mil (‰) deviations relative to the V-SMOW and PDB (PeeDee Belemnite) standards. Error of reproducibility, based on complete analysis of internal standards (including acid digestion) was ± 0.1‰ for $\delta^{13}C$, and ± 0.2‰ for $\delta^{18}O$ (1σ).

Mineralogy

The ore mineral association is pyrite ± chalcopyrite and fahlore [$\sim(Cu,Ag)_{10}(Zn,Fe)_2Sb_4S_{13}$] as major phases, and minor amounts of gold, sphalerite, galena, bournonite-seligmanite ($PbCuSbS_3$–$PbCuAsS_3$), marcasite, and pyrrhotite (Fig. 2b, c). The textural study has revealed the following paragenetic sequence: pyrrhotite → pyrite + gold (pyrite stage) → chalcopyrite + sphalerite + galena → fahlore + marcasite (polymetallic stage). The gangue minerals in the veins are mainly coarse quartz, with minor ankerite occurring after quartz formation (Fig. 2d) and white mica microcrystals (''sericite'') intergrown with quartz (Fig. 2e).

Hydrothermal alteration

Hydrothermal alteration, mainly propylitic type, covers a great area (ca. 30 km^2 wide, Fig. 1b). The primary volcanic mineralogy adjacent to the studied veins has been completely obliterated, and only accessory phases such as apatite remain as relicts. The alteration assemblage, determined by X-ray diffraction and microscopic study, consists largely of quartz and phyllosilicates. These phyllosilicates are mainly fine grained white mica (''illite''), with minor kaolinite (Fig. 3). The (001) mica peak of the untreated sample is non-symmetric, with a widening of the base peak to lower 2θ. This suggests a certain proportion of smectite interstratified

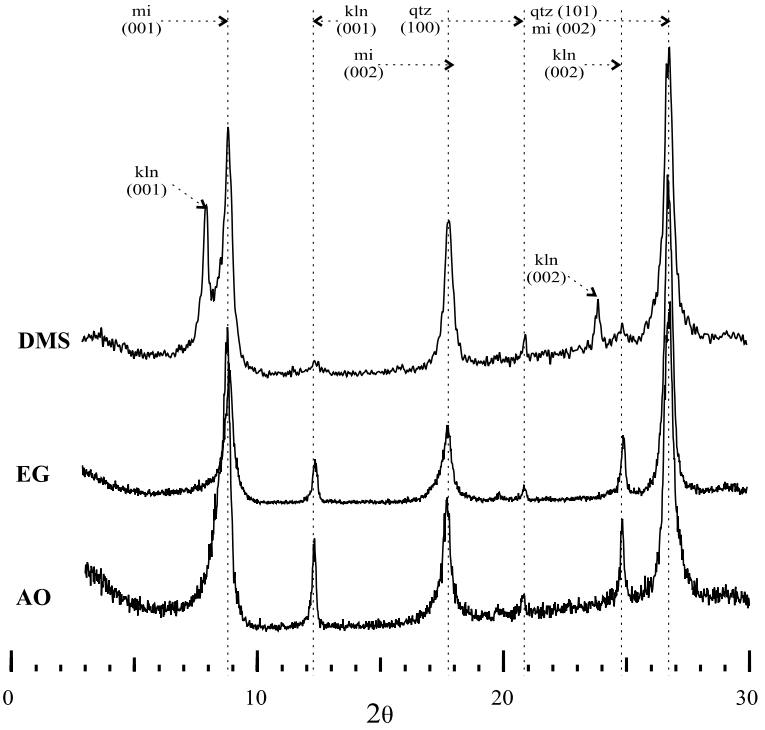

Fig. 3. Oriented powder X-ray diffraction patterns (Cu Kα radiation $\lambda = 0.154$ nm) of the less than 2 μm size fraction of a sample from the hydrothermal alteration zone near an ore vein. The positions of basal peaks of kaolinite (*kln*) and mica (*mi*), and the main quartz (*qtz*) peaks are marked in the figure with vertical dotted lines. Patterns are shown for the air dried (*AO*), ethylene glycol treated (*EG*) and dimethyl sulfoxide treated (*DMS*) sample

layers inside the mica stacks. EPMA analyses (Table 1) reveal the mica is K and (Fe + Mg)-bearing, its composition being dominantly marked by the phengite substitution type $((Fe + Mg)_1Si_1{}^{VI}Al_{-1}{}^{IV}Al_{-1})$ and in lesser proportion by the illite substitution type $(Si_1\square Al^{IV}{}_{-1}K_{-1})$. Figure 4 demonstrates that mica crystals from within the vein have a more muscovitic composition than those from the hydrothermal alteration zones.

Ore mineralogy

Gold occurs as grains of electrum of a few tens of microns in diameter, interstially or in fractures within aggregates of pyrite. Electrum grains have homogeneous composition and do not exhibit chemical zonation in backscattered electron images (Fig. 5a). Their composition is mainly Au with Ag (Ag: 32.38–37.26 at.%, Table 1). Fe is found in electrum analyses in a range from 0.31 to 0.95 at.% (Table 1). Pyrite is coarse, with pentagonal dodecahedral or anhedral crystals up to several centimetres. It commonly has compositional zonation with respect to As, and to a lesser degree, to Co and Ni. The As-rich zones have an irregular band or patch-like morphology and are the expression of a relatively advanced stage of pyrite precip-

Table 1. *Summary of EPMA analyses*

	Mica ($n=13$)				Gold ($n=6$)				Pyrite ($n=41$)				Sphalerite ($n=7$)				Bournonite ($n=4$)				Fahlore ($n=35$)		
wt.%	Min.	Max.	Ave.	wt.%	Min.	Max.	Ave.	wt.%	Min.	Max.	Ave.	wt.%	Min.	Max.	Ave.	wt.%	Min.	Max.	Ave.	wt.%	Min.	Max.	Ave.
SiO_2	48.47	51.59	49.98	Au	76.09	81.25	78.64	Au	0.00	0.13	0.03	S	31.97	33.15	32.87	S	19.65	20.63	20.07	S	23.29	29.06	26.08
Al_2O_3	30.15	32.40	31.12	Ag	21.78	25.45	23.83	Ag	0.00	0.28	0.03	Zn	63.54	65.85	64.88	As	3.44	4.92	4.07	As	0.99	18.99	7.52
TiO_2	0.03	0.19	0.10	S	0.02	0.21	0.11	S	50.27	53.71	52.48	Fe	0.17	1.16	0.91	Sb	18.16	20.73	19.16	Sb	0.55	27.14	18.03
FeO	1.41	2.37	2.07	Bi	0.00	0.12	0.02	Sb	0.00	0.06	0.02	Mn	0.00	0.06	0.04	Fe	0.01	0.03	0.02	Fe	1.77	11.91	5.52
MgO	1.16	1.38	1.28	Fe	0.11	0.33	0.23	Fe	43.79	47.03	46.08	Cd	0.03	0.33	0.28	Cu	13.07	13.21	13.16	Cu	34.34	42.99	39.54
MnO	0.00	0.03	0.02	Te	0.07	0.14	0.10	Co	0.03	0.16	0.07	In	0.00	0.00	0.00	Zn	0.01	0.02	0.01	Zn	0.00	5.69	1.80
CaO	0.14	0.23	0.19	Cu	0.00	0.02	0.01	Ni	0.00	0.09	0.01	Ga	0.00	0.09	0.04	Ag	0.00	0.00	0.00	Ag	0.15	1.31	0.57
K_2O	8.90	10.23	9.48	Hg	0.00	0.00	0.00	Cu	0.00	0.50	0.03	Ge	0.00	0.03	0.01	Hg	0.07	0.21	0.13	Hg	0.20	1.37	0.57
Na_2O	0.08	0.14	0.11	Se	0.00	0.03	0.01	Zn	0.00	0.48	0.02	Cu	0.00	0.21	0.08	Sn	0.00	0.00	0.00	Sn	0.00	0.04	0.01
F	0.00	0.02	0.01	Fineness:	753	789	767	As	0.00	3.60	0.99	Sb	0.00	0.41	0.14	Pb	42.85	44.38	43.52	Pb	0.05	0.27	0.13
Cl	0.01	0.14	0.08	$Au/(Au+Ag)\times1000$								Sn	0.00	0.00	0.00	Bi	0.11	0.16	0.14	Bi	0.00	0.15	0.08
												As	0.00	0.00	0.00								
a.p.f.				at.%				at.%				at.%				at.%				at.%			
Si	3.29	3.38	3.33	Au	62.04	66.16	63.48	Au	0.00	0.03	0.01	S	50.00	50.86	50.25	S	49.54	50.21	49.81	S	43.02	47.92	44.68
^{IV}Al	0.62	0.71	0.67	Ag	32.38	37.26	35.12	Ag	0.00	0.10	0.01	Zn	47.94	49.47	48.65	As	3.62	5.12	4.32	As	0.78	12.85	5.39
^{VI}Al	1.74	1.80	1.78	S	0.10	1.05	0.57	S	65.04	66.70	66.05	Fe	0.15	1.01	0.79	Sb	11.63	13.44	12.53	Sb	0.23	13.03	8.27
Ti	0.00	0.01	0.00	Bi	0.00	0.10	0.02	Sb	0.00	0.02	0.01	Mn	0.00	0.05	0.04	Fe	0.01	0.04	0.03	Fe	1.88	11.27	5.40
Fe	0.08	0.13	0.12	Fe	0.31	0.95	0.65	Fe	32.55	33.70	33.30	Cd	0.01	0.14	0.12	Cu	16.19	16.75	16.48	Cu	28.61	35.14	34.20
Mg	0.11	0.14	0.13	Te	0.08	0.18	0.13	Co	0.00	0.08	0.03	In	0.00	0.00	0.00	Zn	0.01	0.02	0.02	Zn	0.00	4.89	1.55
Mn	0.00	0.00	0.00	Cu	0.00	0.05	0.02	Ni	0.00	0.06	0.01	Ga	0.00	0.06	0.02	Ag	0.00	0.00	0.00	Ag	0.07	0.72	0.29
$^{VI}\Sigma$	2.01	2.03	2.03	Hg	0.00	0.00	0.00	Cu	0.00	0.32	0.02	Ge	0.00	0.02	0.01	Hg	0.03	0.09	0.05	Hg	0.06	0.36	0.15
Ca	0.01	0.02	0.01	Se	0.00	0.06	0.02	Zn	0.00	0.30	0.02	Cu	0.00	0.16	0.06	Sn	0.00	0.00	0.00	Sn	0.00	0.02	0.00
K	0.74	0.88	0.81	$Au/$	0.63	0.67	0.64	As	0.00	1.96	0.54	Sb	0.00	0.17	0.06	Pb	16.64	16.78	16.72	Pb	0.01	0.08	0.04
Na	0.01	0.02	0.01	$(Au+Ag)$								Sn	0.00	0.00	0.00	Bi	0.04	0.06	0.05	Bi	0.00	0.04	0.02
Inter-layer	0.77	0.91	0.83									As	0.00	0.00	0.00	$As/(As+Sb)$	0.21	0.31	0.26	$As/(As+Sb)$	0.06	0.98	0.40
F	0.00	0.03	0.02													Sb)				$Zn/(Zn+Fe)$	0.00	0.72	0.22
Cl	0.00	0.00	0.00																	$Ag/(Ag+Cu)$	0.00	0.02	0.01

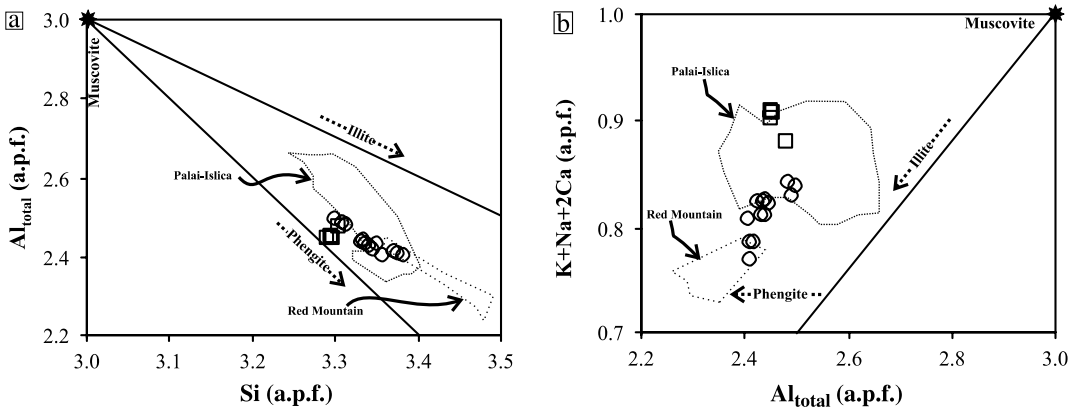

Fig. 4. Binary diagrams, (**a**) Si *vs.* Al_{total} and (**b**) Al_{total} *vs.* $K + Na + 2Ca$ in atoms per formula (normalized to $O_{10}(OH)_2$), showing the composition of mica determined by EPMA analyses from the ○ hydrothermal alteration and □ vein proper. Shown with references to mica from other epithermal Au deposits: Palai-Islica, Spain (*Carrillo-Rosúa*, 2005); Red Mountain, USA (*Bove* et al., 2002)

itation. The As-bearing pyrite zones do not directly host gold grains (Fig. 5). The maximum As content is 1.96 at.%, while Co and Ni are typically less than 0.1 at.% (Table 1). The increase of As concentration in pyrite is mainly associated with a S decrease (Fig. 6a), but there is also some suggestion of relationship with an Fe decrease (Fig. 6b).

Gold and pyrite precipitation was followed by a base metal sulfide-bearing stage. Sphalerite is colourless or yellowish (under microscopic examination) and Fe-poor (maximum of 1.01 at.%), with a Cd content around 0.14 at.% (Table 1). Bournonite-seligmanite is richer in Sb than As (21–31% seligmanite component, Table 1). Fahlore is a very abundant phase in the latest stage of ore precipitation, and shows a marked zonation pattern (Fig. 7a, b). The composition of fahlore (Table 1) ranges between tennantite-rich (79% tennantite) and tetrahedrite-rich (94% tetrahedrite), with tetrahedrite (Sb-rich) being the more common. The Ag content (Table 1) is low (0.07–0.72 at.%), but with higher concentrations correlating with high Sb content (Fig. 8a). Such feature is commonly observed in different types of hydrothermal systems including epithermal gold-bearing deposits (e.g., *Johnson* et al., 1986; *Ebel* and *Sack*, 1991; *Cook* et al., 1998; *Carrillo-Rosúa*, 2005). The Fe and Zn contents of the fahlore are very variable (1.88–11.27 at.%, 0.00–4.89 at.%, respectively), and show no apparent correlation with Sb content (Fig. 8b, c). Fahlore precipitated in three stages (Fig. 7a, b). During the first stage fahlore with high Zn, Sb and Ag contents formed. This fahlore is volumetrically the most important. In a second stage, chemically variable but generally Sb, and Ag-poor fahlore was deposited. The third stage fahlore is characterized by the lowest Zn content but the highest Fe content, and Sb, Ag contents are slightly lower than in the first stage (Fig. 8c). Thus, the main differences between these three fahlore zones are the $As/(As + Sb)$ ratio, with higher values in the middle zone, and the $Zn/(Zn + Fe)$ ratio which decreases from the innermost to the outermost zone.

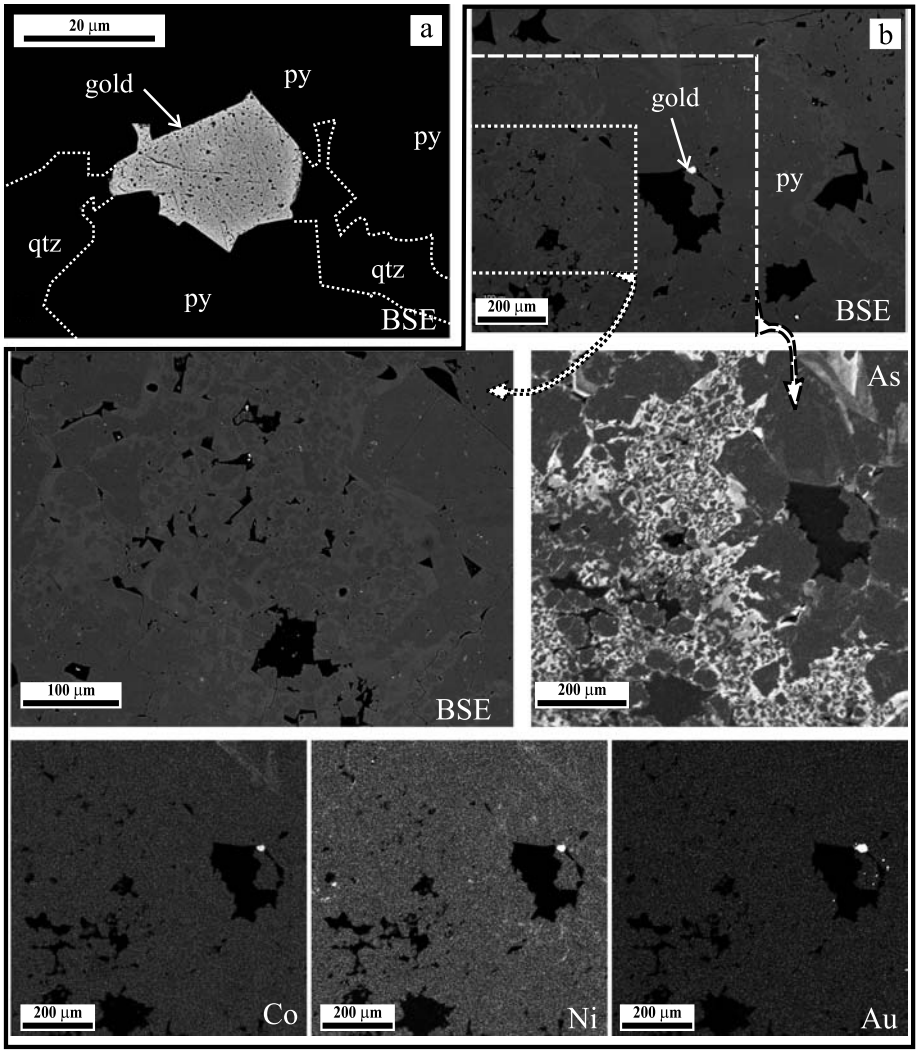

Fig. 5. Backscattered electron (BSE) and X-ray (As, Co, Ni and Au) images of pyrite hosting an unzoned gold grain. Pyrite shows a strong zonation mainly due As enrichment. The As-rich zone has an irregular morphology and is predated but also postdated by some As-free pyrite

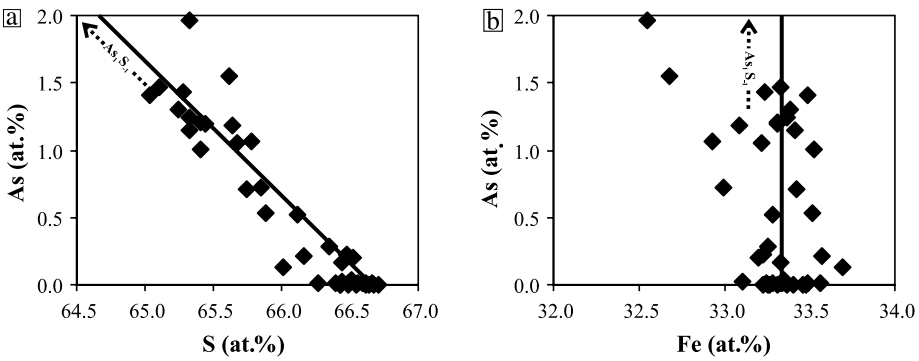

Fig. 6. Binary diagrams showing the composition of pyrite expressed as atomic percent: (**a**) S *vs.* As and (**b**) Fe *vs.* As. *Thick lines* show the exchange vector S_1As_{-1}

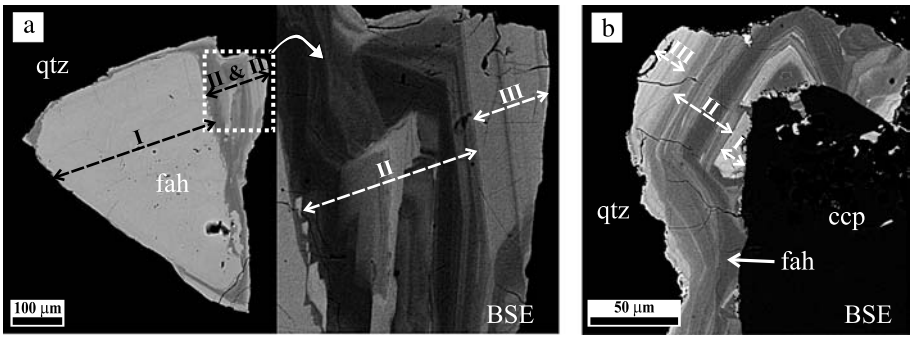

Fig. 7. Backscattered electron (BSE) images of two fahlore (fah) crystals (**a**, **b**) showing an oscillatory zonation pattern. Three main zones, corresponding to three consecutive precipitation stages (I–III), have been distinguished

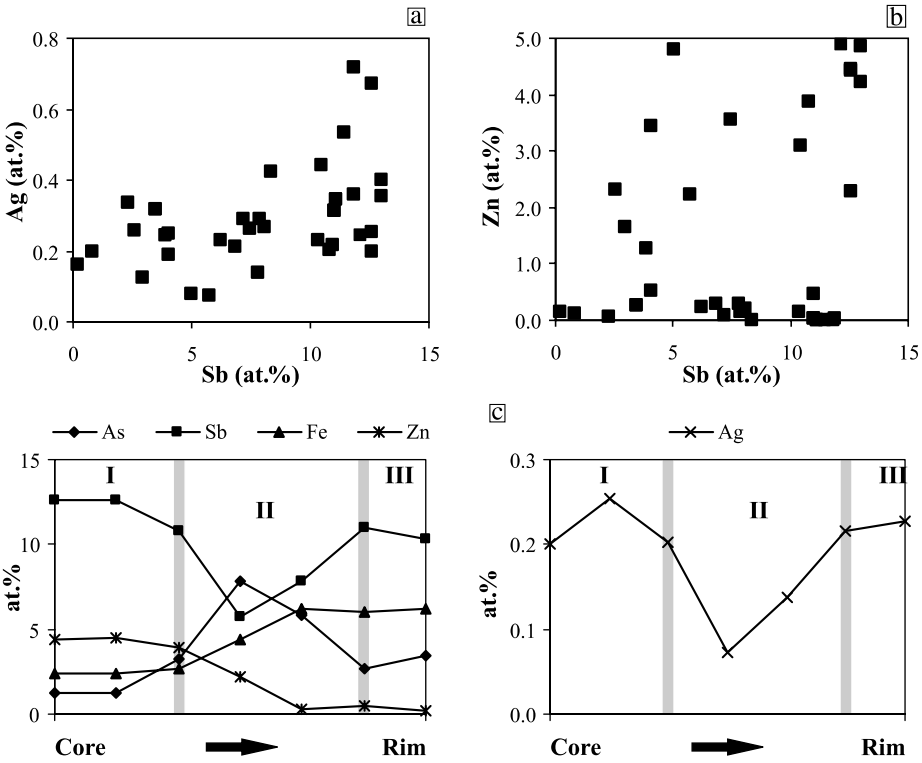

Fig. 8. Binary diagrams showing the composition of fahlore expressed as atomic percent: (**a**) Sb *vs.* Ag and (**b**) Sb *vs.* Zn. (**c**) Cross section of a fahlore crystal showing the composition of the three zones I, II and III as in Fig. 7

Fluid inclusion microthermometry

The petrographic study of fluid inclusions in quartz from mineralized veins shows isolated cavities or small random groups, which are characteristic of primary fluid inclusions (*Roedder*, 1984). All fluid inclusions found in the quartz and ankerite are two-phase (L + V), <20 µm in size, with L/(L + V) always higher than 0.8. The microthermometric study of fluid inclusions in quartz shows temperatures of first melting (Te) around −50 °C indicating that the fluids can be represented by the

system H_2O–NaCl–$CaCl_2$(–KCl) (*Shepherd* et al., 1985). During freezing, no phase changes in the vapour phase were observed, suggesting that the amount of other gases such as CO_2 present in the vapour phase is negligible. The final melting temperatures range from −0.9 to −4.3 °C which corresponds to a salinity range between 1.6 and 6.9 wt.% NaCl eq., with an average of 4 wt.% NaCl eq. The temperatures of homogenization range between 130 and 352 °C, with the majority between 150 and 250 °C. A wide range of salinities coincides with a narrow range of homogenization temperatures. Fluid inclusions with homogenization temperatures above 250 °C are scarce and are moderately saline (Fig. 9).

Stable isotope geochemistry

A stable isotope study has been performed in silicates, carbonates and sulfides; results are listed in Table 2. Two silicate samples were analyzed: coarse quartz from a mineralized vein and a mixture of phyllosilicates (mica ± kaolinite) from the hydrothermal alteration. The $\delta^{18}O$ values obtained for both samples are quite high (19.5‰ for quartz and 12.8‰ for mica ± kaolinite), while δD values of the phyllosilicates are strongly negative (−100‰). The deduced $\delta^{18}O$ ranges of the fluid in equilibrium with different minerals are: 4.2–10.6‰ (quartz) and 2.3–6.9‰ (mica), while the deduced δD of the fluid in equilibrium with mica is −95 to −75‰ (Fig. 10). These values have been calculated on the basis of the range of tempera-

Table 2. *Stable isotope analyses of silicate, carbonate and sulfide minerals from the El Dorado deposit*

Mineral	$\delta^{18}O_{VSMOW}$ (‰)	δD_{VSMOW} (‰)	$\delta^{13}C_{PDB}$ (‰)	$\delta^{34}S_{CDT}$ (‰)
Quartz	19.5			
Mica ± kaolinite	12.8	−100		
Ankerite	18.6		−2.3	
Pyrite				0.2
Chalcopyirte				0.9
Fahlore				2.6

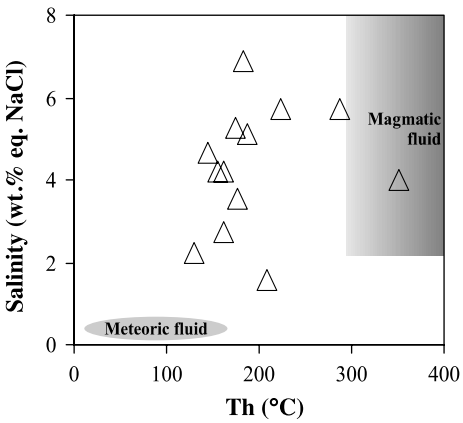

Fig. 9. Th (temperature of homogenization) *vs.* salinity diagram of fluid inclusions hosted in quartz veins. The hypothetical compositions of magmatic and meteoric waters plotted according to *Hedenquist* et al. (1998) and *Naden* et al. (2005)

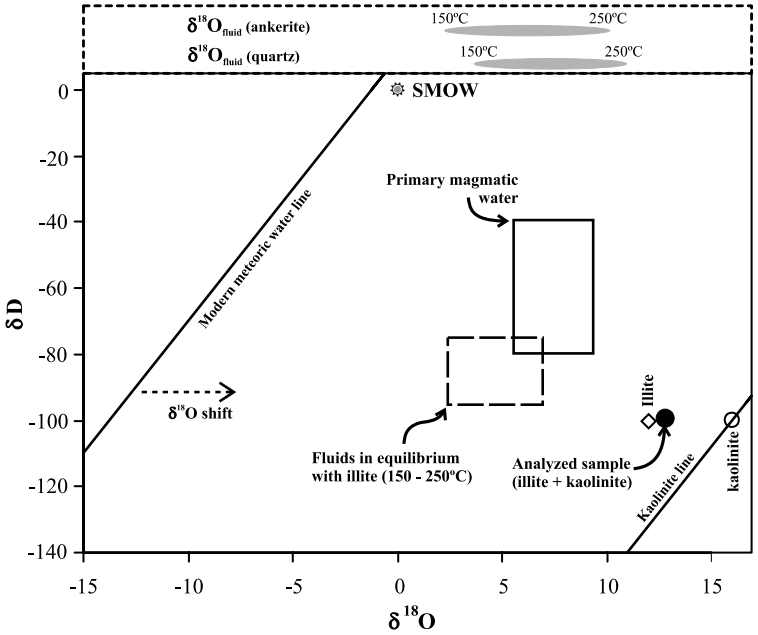

Fig. 10. δD_{fluid} *vs.* $\delta^{18}O_{fluid}$ (‰, in respect to V-SMOW) calculated from phyllosilicates from the hydrothermal alteration, and $\delta^{18}O_{fluid}$ calculated from quartz and ankerite from the veins from the El Dorado deposit. The fractionation factors used to calculate fluid signature are: *Matsuhisa* et al. (1979) for quartz; *Zheng* (1999) for ankerite; *Sheppard* and *Gilg* (1996) and *Vennemann* and *O'Neil* (1996) for illite. Also shown for reference are magmatic waters (*Taylor*, 1974), the kaolinite line (*Savin* and *Epstein*, 1970), the modern meteoric water line (*Craig*, 1961). Kaolinite is assumed to be supergene being illite isotopic signature calculated by mass balance

ture deduced from the fluid inclusion study: 150–250 °C, and fractionation equations of *Matsuhisa* et al. (1979), *Sheppard* and *Gilg* (1996) and *Vennemann* and *O'Neil* (1996). Late ankerite has a $\delta^{13}C$ of −2.3‰ and $\delta^{18}O$ of 18.6‰. The $\delta^{18}O$ of the fluid in equilibrium with ankerite is between 3.3 and 9.7‰ (at 150–250 °C, and with *Zheng* (1999) fractionation factor), within the range of the silicates. Primary sulfides have slightly positive and homogeneous sulfur $\delta^{34}S$ values (0.2–2.6‰), with $\delta^{34}S$ of fahlore > chalcopyrite > pyrite (Table 2).

Discussion

The mineralogical study has revealed the existence of two main mineralization stages in the El Dorado. An early pyrite-rich stage with precious metals, and a later polymetallic, Cu-rich stage. The high As content of pyrite, and its concentration in discrete zones in pyrite (bands or patches), is a feature typical of epithermal environments (e.g., *Christiansen* et al., 1983; *Hulen* and *Nielson*, 1986; *Fleet* et al., 1989; *Griffin* et al., 1991; *Cline*, 2001; *Carrillo-Rosúa* et al., 2003; *Pals* et al., 2003), although experimental studies (*Clark*, 1960) show that only minor amounts of As (up to 0.5 wt.%) are stable in pyrite, and are an expression of disequilibrium and metastable conditions, also typical of epithermal systems. The As was probably incorporated in a metastable solid solution in the S sites, related to very As-rich

layers with ''marcasite-like'' structure (*Fleet* et al., 1989; *Simon* et al., 1999) or as clusters with a lower As content in the pyrite structure (*Savage* et al., 2000). We cannot rule out the occurrence of some non-stochiometric As, maybe as a result of strong disequilibrium conditions (*Carrillo-Rosúa* et al., 2003), in the highest As-rich pyrites, which also have lower Fe content (Fig. 6b). Such As-rich pyrite is known to host ''invisible gold'' (e.g., *Reich* et al., 2005, and references therein), mostly in Carlin type-deposits (e.g., *Cook* and *Chryssoulis*, 1990; *Fleet* and *Mumin*, 1997; *Asadi* et al., 1999; *Cline*, 2001), but also in volcanic-hosted epithermal gold deposits (up to 11000 ppm Au, *Pals* et al., 2003). In the case of the El Dorado deposit, EPMA analyses are insufficient to quantify the gold content in pyrite: most of the analyses are below 0.06 wt.%, i.e., the detection limit of gold. Nevertheless, no difference in Au content between As-rich and As-poor pyrite has been found.

Gold at the El Dorado deposit is present as electrum grains along fractures in pyrite or interstitially within aggregates of pyrite crystals. This relationship suggests that gold precipitated after the initial formation of pyrite, which would has drastically decreased the sulfur content of the hydrothermal fluid. Since gold (and silver) would be mainly transported by sulfide complexes at epithermal conditions (e.g., *Seward* and *Barnes*, 1997), and a fS_2 drop may lead to gold precipitation (e.g., *Gammons* and *William-Jones*, 1995), the electrum formation may thus has been related to pyrite precipitation as has been argued for others epithermal deposits (*Carrillo-Rosúa* et al., 2002). The electrum has a high Au content, with some alloyed Ag. The Fe content of the electrum recorded in the analyses (Table 1) could be due to secondary fluorescence of the host pyrite; it is known that the Fe$K\alpha$ line could be produced by the Au$L\alpha$ radiation during analysis (*Healey* and *Petruk*, 1990). The low Cu content is consistent with the interpretation of the El Dorado as an epithermal system base on data reported by *Palacios* et al. (2001) for Au-Ag alloys from several epithermal and porphyry Andean gold deposits. The fineness ($Au/(Au+Ag)\times 1000$, in wt.%) values of the El Dorado electrum (Table 1) are within the range of 720–980 defined by *Morrison* et al. (1991) as typical of the andesitic environment, and in the upper part of the range for ''adularia-sericite'' type environments (0–880), rather than in the range for ''acid-sulfate'' environments (900–1000) according to the same authors.

The later polymetallic stages are characterized mainly by Cu-bearing phases (chalcopyrite >> fahlore > bournonite(-seligmanite)). Sphalerite is also present, and has a Fe content, in the edge of sphalerite from typical low-sulfidation deposits, commonly 1–4 mol.% FeS (*Heald* et al., 1987) and compatible with intermediate-sulfidation deposits (e.g., *Simmons* et al., 2005). The fahlore exhibits great variability in chemistry, mainly in $As/(As+Sb)$ and $Zn/(Zn+Fe)$ ratios, resulting in a characteristic zonation pattern (Fig. 7). The zonal variations reflect changes in the physico-chemical conditions of the hydrothermal fluid during the polymetallic mineralization stage. Some of these chemical variations, e.g., Fe increase with time, may reflect a cooling of the fluid (e.g., *Chutas* and *Sack*, 2004), since the Ag content did not change very significantly. The low content of Ag in fahlore, often a typical Ag-bearing phase (e.g., *Johnson*, 1986), indicates a low concentration of Ag in the hydrothermal system during the base metal stage.

The mineralization is associated with a hydrothermal alteration assemblage containing white mica and minor kaolinite. The mica is K-bearing (Table 1) and

has a composition defined more by phengite substitution ($(Fe + Mg) + Si \rightarrow {}^{VI}Al + {}^{IV}Al$) than by illite substitution ($Si + \text{vacancy} \rightarrow Al^{IV} + K$). Its composition is similar to micas found in other epithermal volcanic-hosted deposits (Fig. 4). The micas (''sericite'') are also present in the quartz veins, either directly precipitated from the fluid or incorporated in the veins after replacement of plagioclase phenocrysts. They have a more muscovite-like composition with, in particular, a smaller illite component compared to the micas in the altered wall-rocks. This chemical feature may indicate that the micas show an approach to chemical equilibrium greater in the veins than in the altered wall-rocks. The reason for that is probably due to a higher water-rock interaction rather than to a different thermodynamic condition among hydrothermal alteration and the veins (e.g., temperature). Mica compositions would be expected to be reached in mica crystals at 300 °C if equilibrium conditions existed between fluids and mineral products (e.g., *Abad* et al., 2003).

The kaolinite is thought to be of a supergene origin. The presence of relicts of apatite crystals indicate the absence of a percolating acidic hydrothermal fluid that would be required during the hypogene stage for the formation of hydrothermal kaolinite, a typical feature of high-sulfidation deposits (e.g., *Heald* et al., 1987; *Hedenquist* et al., 2000). The hydrothermal alteration assemblage around the El Dorado ore veins is consistent with close to neutral hydrothermal fluids. Smectite which is intestratified with mica, as deduced from X-ray analysis (Fig. 3), could also have formed during supergene processes.

The homogenization temperature values of fluid inclusions in quartz indicate that the minimum temperature of hydrothermal fluids were mostly between 150 and 250 °C. True temperatures of formation would be only slightly superior (<50 °C) to temperatures of homogenization, since the shallow emplacement of the deposit, the pressure correction being small. This temperature range is in agreement with typical temperatures in epithermal systems (e.g., *Simmons* et al., 2005). The salinity of the hydrothermal fluid was variable, but greater than 1.6 wt.% NaCl eq. This rules out that the hydrothermal system was dominated by meteoric water; in this case very low salinities would be expected (<1 wt.% NaCl eq., e.g., *Naden* et al., 2005). Salinities at the El Dorado would only be compatible with an origin from meteoric waters if excessive boiling or large-scale rock buffering of fluid compositions had occurred (e.g., *Sillitoe* and *Hedenquist*, 2003). Boiling, rather than simple cooling of moderately saline rock-exchanged meteoric waters, could explain the ''vertical'' trend observed in the homogenization temperature *vs.* salinity diagram (Fig. 9). But boiling is not supported by petrographic evidence, such as heterogeneous entrapment of fluid inclusions. An alternative and more convincing explanation is the presence of magmatic water, which could have salinity in the range of 2–10 wt.% NaCl eq. (e.g., *Hedenquist* et al., 1998). Following this explanation, the fluid inclusion data for quartz are consistent with a mixing process between magma-derived and meteoric fluids.

The oxygen and hydrogen isotope signatures for the hydrothermal fluid deduced from quartz, phyllosilicate and carbonate isotope analyses are also consistent with a hydrothermal fluid containing a magmatic water component (Fig. 10). A purely meteoric source for the hydrothermal fluids is considered unlikely, although part of the heavy oxygen isotope signature may be explained by water-rock interaction. Similar isotope signatures for hydrothermal fluids have been documented,

for example, for mesothermal Korean precious metal deposits (*Shelton* et al., 1988). Fluids precipitating carbonates maybe had a slightly lower $\delta^{18}O$ signature than those precipitating silicates. This could be reflecting the participation of a higher proportion of meteoric water in the late stage of the mineralization, and hypothetically may also suggest leaching of marine Lower Cretaceous carbonates, since the measured $\delta^{13}C$ is maybe too heavy to be solely magmatic derived. The $\delta^{13}C$ of magmatic carbon is typically $-5‰$, although it can range between -7 and $-2‰$ (*Deines* et al., 1991; *Cartigny* et al., 1998).

The $\delta^{34}S$ values of the sulfides ranging from 0.2 to 2.6‰ are at the heavier end of the range reported for Andean epithermal/magmatic systems (e.g., Pascua-Lama: -5 to $-3‰$, *Deyell* et al., 2005; El Salvador, Chuquicamata, Río Blanco-Los Bronces: -10 to 3‰, *Field* and *Gustafson*, 1976; *Sasaki* et al., 1984; *Frikken* et al., 2005). There is little doubt however that the source of sulfur in the system was dominated by magmatic sulfur. This magmatic sulfur could be derived from the leaching of volcanic rocks, or more probably, from a fluid exsolved from the magma since a magmatic component in the hydrothermal fluids has been deduced. Incorporation of biogenic sulfide (either within the magmatic system, or during fluid circulation) would likely lead to a decrease in $\delta^{34}S$, which we do not see at the El Dorado. There is a suggestion that $\delta^{34}S$ increased through the paragentic sequence at the El Dorado (Table 2), but we do not propose to discuss this further on the basis of only three data points.

The location of the El Dorado deposit is consistent with an age of formation between the Upper Cretaceous and the Paleocene. During this period, several epithermal deposits were formed along the Coastal Range and Precordillera of Chile from north of Antofagasta (e.g., Faride) to south of Santiago (e.g., El Tigre). Among these deposits, only the El Guanaco deposit could be classified as high sulfidation (*Camus*, 1990). Also for the El Dorado deposit, the high-sulfidation model is rejected whereas the intermediate-sulfidation model fits well with the observed mineralogical and geochemical features. Thus, Upper Cretaceous and Paleocene terrains constitute an interesting target for low-sulfidation deposits but also for intermediate-sulfidation deposits (some of the deposits earlier classified as low – e.g., *Camus*, 1990 – maybe fit better with an intermediate classification but this classification did not exist at the time that these deposits were characterized). This type of deposits, rather than high-sulfidation deposits, has formed as a result of extensional tectonism during Late Cretaceous and Paleocene.

Conclusions

This work provides a first insight into the El Dorado deposit and its ore potential. Pyrite and chalcopyrite are the main sulfides. All visible gold is related to pyrite, occurring either in fractures or within aggregates. Free gold grains occur in the form of electrum, with a fineness of 753–781 at the lower end of the range typical of andesitic environments, and outside of the high-sulfidation field as defined by *Morrison* et al. (1991). The host pyrite has a significant As content (up to 1.96 at.%), concentrated in bands and patches of primary origin, but neither the As-rich, nor As-poor areas contain significant ‘‘invisible gold’’. The ore is Cu-rich and Au–As–Sb–Zn–Pb-bearing, which is a feature typical of epithermal deposits

associated with intermediate-acid magmatism. The ore textures suggest that gold precipitation occurred at the end of an early pyrite-dominated stage, with Cu, Sb, Zn, and Pb precipitated during a later base metal-dominated stage. Arsenic is present throughout the mineralization sequence. The mineral chemistry of the ore minerals, such as pyrite and fahlore, also reveal a complex evolution of the mineralizing fluids.

The range of Th (130–352 °C, with most data between 150 and 250 °C) is consistent with an epithermal environment. The salinity and stable isotope signature of the ore-forming fluids suggest contributions of both meteoric and magmatic fluids, with a mixing process between both types of fluids possibly related to mineralization. The ore mineralogy and mineral chemistry, the control of mineralization by veins, the types of hydrothermal alteration, and the composition and temperature range of the fluids are consistent with the interpretation that the El Dorado deposit is an epithermal intermediate-sulfidation deposit.

Acknowledgements

This work has been supported by the Spanish project BTE-2003-06265 (Ministry of Science and Technology/Ministry of Education and Science and FEDER), Research Group RNM131 of the Junta de Andalucía, "Departamento de Investigación y Desarrollo" (DI) I001-99/2 project of the University of Chile and the CSIC-Universidad de Chile project CSIC/2001/02-08. SUERC is funded by NERC and the consortium of Scottish Universities. J. Carrillo-Rosúa thanks MEC postdoctoral grant. The authors are grateful to Alonso Toledo for his help during field work and also thank G. Pineda (SERNAGEOMIN, Chile) for the providing access to geological information of the studied area. An early version of the manuscript improved with the comments of V. Maksaev, R. Tosdal and W. Vivallo. Reviews by R. Both and T. Bissig clearly helped to improve this manuscript.

References

Abad I, Nieto F, Gutiérrez-Alonso G (2003) Textural and chemical changes in slate-forming phyllosilicates across the external-internal zones transition in the in the low-grade metamorphic belt of the NW Iberian Variscan Chain. Schweiz Mineral Petrogr Mitt 83: 63–80

Aguirre L, Egert E (1965) Cuadrángulo Quebrada Marquesa, provincia de Coquimbo. Carta Geológica de Chile, Instituto de Investigaciones Geológicas, 15, Santiago, 92 pp

Asadi HH, Voncken JHL, Hale M (1999) Invisible gold at Zarshuran, Iran. Econ Geol 94: 1367–1374

Bove DJ, Eberl DD, McCarty DK, Meeker GP (2002) Characterization and modelling of illite crystal particles and growth mechanism in a zoned hydrothermal deposit, Lake City, Colorado. Am Mineral 87: 1546–1556

Camus F (1990) The geology of hydrothermal gold deposits in Chile. J Geochem Explor 36: 187–232

Carrillo-Rosúa FJ (2005) El depósito epitermal de oro-cobre Palai-Islica (Carboneras, Almería). Mineralogía, geoquímica y metalogenia. Ph.D. Thesis, Univ Granada, 421 pp

Carrillo-Rosúa FJ, Morales Ruano S, Fenoll Hach-Alí P (2002) The three generations of gold in the Palai-Islica epithermal deposit, Southeastern Spain. Can Mineral 40: 1465–1481

Carrillo-Rosúa FJ, Morales Ruano S, Fenoll Hach-Alí P (2003) Iron sulphides at the epithermal gold–copper deposit of Palai-Islica (Almería, SE of Spain). Mineral Mag 67: 1059–1080

Cartigny P, Harris JW, Javoy M (1998) Eclogitic diamond formation at Jwaneng. No room for a recycled component. Science 280: 1421–1424

Christiansen OD, Capuano RA, Moore JN (1983) Trace element distribution in an active hydrothermal system, Roosevelt Hot Spring thermal area, Utah. J Volcanol Geotherm Res 16: 99–129

Chutas NI, Sack RO (2004) Ore genesis at La Colorada Ag–Zn–Pb deposit in Zacatecas, Mexico. Mineral Mag 68: 923–937

Clark LA (1960) The Fe–As–S system: phase relations and applications. Econ Geol 55: 1345–1381

Cline JS (2001) Timing of gold and arsenic sulfide mineral deposition at the Getchell Carlin-type gold deposit, north-central Nevada. Econ Geol 96: 75–89

Cook NJ, Chryssoulis SL (1990) Concentrations of ''invisible gold'' in the common sulphides. Can Mineral 28: 1–16

Cook NJ, Spry PG, Vokes FM (1998) Mineralogy and textural relationships among sulphosalts and related minerals in the Bleikvassli Zn–Pb–(Cu) deposit, Nordland, Norway. Mineral Deposita 34: 35–56

Craig H (1957) Isotopic standards and isotopic correction factors for mass spectrometric analysis of carbon dioxide. Geochim Cosmochim Acta 12: 133–149

Craig H (1961) Isotopic variations of meteoric waters. Science 133: 1702–1703

Deines P, Harris JW, Gurney JJ (1991) The carbon isotopic composition and nitrogen content of lithospheric and asthenospheric diamonds from the Jagersfontein and Koffiefontein kimberlite, South Africa. Geochim Cosmochim Acta 55: 2615–2625

Deyell CL, Leonardson R, Rye RO, Thompson JFH, Bissig T, Cooke DR (2005) Alunite in the Pascua-Lama high-sulfidation deposit: constraints on alteration and ore deposition using stable isotope geochemistry. Econ Geol 100: 131–148

Donnelly T, Waldron S, Tait A, Dougans J, Bearhop S (2001) Hydrogen isotope analysis of natural abundance and deuterium-enriched waters by reduction over chromium on-line to a dynamic dual inlet isotope-ratio mass spectrometer. Mass Spectrom 15: 1297–1303

Ebel DS, Sack R (1991) Arsenic-silver incompatibility in fahlore. Mineral Mag 55: 521–528

Emparan C, Pineda G (1999) Area Condoriaco-Rivadavia, Región de Coquimbo. Servicio Nacional de Geología y Minería, Mapas Geológicos, No 18, 1 mapa escala 1:100.000, Santiago

Emparan C, Pineda G (2000a) Area La Serena-La Higuera, Región de Coquimbo. Servicio Nacional de Geología y Minería, Mapas Geológicos, No 12, 1 mapa escala 1:100.000, 1 anexo, Santiago

Emparan C, Pineda G (2000b) Estratigrafía y geocronología U–Pb y K–Ar de los sistemas volcánicos del Cretácico Superior-Paleógeno en la zona de Condoriaco-Rivadavia, Región de Coquimbo. In: IX Congreso Geológico Chileno, Puerto Varas (Chile), Vol. 1, pp 782–786

Emparan C, Pineda G (2007) Geología del área de Andacallo-Puerto Aldea Región de Coquimbo. Servicio Nacional de Geología y Minería. Carta Geológica de Chile, 1 mapa escala 1:100.000, Santiago (in press)

Field CW, Gustafson LB (1976) Sulfur isotopes in the porphyry copper deposit at El Salvador, Chile. Econ Geol 71: 1533–1548

Fleet ME, McLean PJ, Barbier J (1989) Oscillatory-zoned As-bearing pyrite from strata-bound and stratiform gold deposits: an indicator or ore fluid evolution. In: *Keays RR*, et al (eds) The geology of gold deposits: the perspective in 1988. Econ Geol Monogr 6: 356–362

Fleet ME, Mumin AH (1997) Gold-bearing Arsenian pyrite and marcasite and arsenopyrite from Carlin trend gold deposits and laboratory synthesis. Am Mineral 82: 182–193

Frikken PH, Cooke DR, Walshe JL, Archibald D, Skarmeta J, Serrano L, Vargas R (2005) Mineralogical and isotopic zonation in the Sur–Sur tourmaline breccia, Río Blanco-Los Bronces Cu-Mo Deposit, Chile: implications for ore genesis. Econ Geol 100: 935–961

Gammons CH, William-Jones AE (1995) Hydrothermal geochemistry of electrum. Thermodynamic constraints. Econ Geol 90: 420–432

Griffin WL, Ashley PM, Ryan SG, Sie SH, Suter GF (1991) Pyrite geochemistry in the North Arm epithermal Ag–Au deposit, Queensland, Australia: a proton-microprobe study. Can Mineral 29: 185–198

Heald P, Foley NK, Hayba DO (1987) Comparative anatomy of volcanic-hosted epithermal deposits: acid-sulfate and adularia-sericite types. Econ Geol 82: 1–26

Healey RE, Petruk W (1990) Petrology of Au–Ag–Hg alloy and ''invisible'' gold in the Trout Lake massive sulfide deposit, Flin Flon, Manitoba. Can Mineral 28: 189–206

Hedenquist JW, Arribas A Jr, Reynolds TJ (1998) Evolution of an intrusion-centred hydrothermal system: far Southeast-Lepanto porphyry and epithermal Cu–Au deposits, Philippines. Econ Geol 93: 373–403

Hulen JB, Nielson DL (1986) Hydrothermal alteration in the Baca geothermal system, Redondo dome, Valles Caldera, New Mexico. J Geophys Res 91: 1867–1886

Johnson NE, Craig JR, Rimstidt JD (1986) Compositional trends in tetrahedrite. Can Mineral 24: 385–397

Jorquera R (2005) Yacimientos metalíferos del area Condoriaco-Rivadavia. Región de Coquimbo. Unpublished report, Servicio Nacional de Geología y Minería, 20 pp

Mathsuhisa Y, Goldsmith HJR, Clayton RN (1979) Oxygen isotopic fractionation in the system quartz-albite-anorthite-water. Geochim Cosmochim Acta 43: 1131–1140

Morata D, Aguirre L (2003) Extensional Lower Cretaceous volcanism in the Coastal Range (29°20′–30°S), Chile: geochemistry and petrogenesis. J South Am Earth Sci 16: 459–476

Morata D, Aguirre L, Belmar M, Morales S, Parada MA, Martínez M, Carrillo J (2003) Geochemical evolution of the Cretaceous magmatism in the Coastal Range of the La Serena (30°S). In: X Congreso Geológico Chileno CD abstracts, Concepción, 5 pp

Morrison GW, Rose WJ, Jaireth S (1991) Geological and geochemical controls on the silver content (fineness) of gold in gold-silver deposits. Ore Geol Rev 6: 333–364

Naden J, Killias SP, Darbyshire DPF (2005) Active geothermal system with entrained seawater as modern analogs for transitional volcanic-hosted massive sulfide and continental magmato-hydrothermal mineralisation: the example of Milos Island, Greece. Geology 33: 541–544

Ohmoto H, Goldhaber MB (1997) Sulfur and carbon isotopes. In: *Barnes HL* (ed) Geochemistry of hydrothermal ore deposits, 3rd edn. John Wiley & Sons, New York, pp 517–611

Palacios C, Herail G, Townley B, Maksaev V, Sepúlveda F, Parseval P, Rivas P, Lahsen A, Parada MA (2001) The composition of gold in the Cerro Casale gold-rich porphyry deposit, Maricunga belt, northern Chile. Can Mineral 39: 907–915

Pals DW, Spry PG, Chryssoulis S (2003) Invisible gold and tellurium in arsenic-rich pyrite from the Emperor gold deposit, Fiji: implications for gold distribution and deposition. Econ Geol 98: 479–493

Pineda G, Emparan C (1997) Nuevos antecedentes de la estratigrafía y geocronología cretácica del norte del río Elqui: evidencias de tectónica extensional. In: VIII Congreso Geológico Chileno, Antofagasta, pp 215–219

Potter RW, Clayne MA, Brown DL (1978) Freezing point depression of aqueous sodium chloride solutions. Econ Geol 73: 284–285

Pouchou JL, Pichoir F (1984) Un nouveau modèle de calcul pour la microanalyse quantitative per spectrométrie de rayons X. La Reserche Aèrospatiale 3: 167–192

Reich M, Kesler SE, Utsunomiya S, Palenik CS, Chryssoulis S, Ewing RC (2005) Solubility of gold in arsenian pyrite. Geochim Cosmochim Acta 69: 2781–2796

Robinson BW, Kusakabe M (1975) Quantitative preparation of SO_2 for $^{34}S/^{32}S$ analyses from sulfides by combustion with cuprous oxide. Anal Chem 47: 1179–1181

Roedder E (1984) Fluid inclusions. In: *Ribbe PH* (ed) Reviews in mineralogy, Vol. 12, 644 pp
Sasaki A, Ulriksen C, Sato K, Ishihara S (1984) Sulphur isotope reconnaissance of porphyry copper and manto type deposits in Chile and the Philippines. Bull Geol Surv Japan 35: 615–622
Savage KS, Tingle TN, O'Day PA, Waychunas GA, Bird DK (2000) Arsenic speciation in pyrite and secondary weathering phases, Mother Lode Gold District, Tuolumne County, California. Appl Geochem 15: 1219–1244
Savin SM, Epstein S (1970) The oxygen and hydrogen isotope geochemistry of clay minerals. Geochim Cosmochim Acta 34: 43–64
SERNAGEOMIN (1982) Mapa Geológico de Chile, escala 1:1.000.000
Seward TM, Barnes HL (1997) Metal transport by hydrothermal ore fluids. In: *Barnes HL* (ed) Geochemistry of hydrothermal ore deposits, 3rd edn. John Wiley & Sons, New York, pp 435–486
Sharp ZD (1990) A laser-based microanalytical method for the in situ determination of oxygen isotope ratios in silicates and oxides. Geochim Cosmochim Acta 54: 1353–1357
Shelton KL, So CS, Chang JS (1988) Gold-rich mesothermal vein deposits of the Republic of Korea: geochemical studies of the Jungwon gold area. Econ Geol 83: 1221–1237
Shepherd T, Rankin AH, Alderton DHM (1985) A practical guide to fluid inclusion studies. Blackie, Glasgow and London, 239 pp
Sheppard SMF, Gilg HA (1996) Stable isotope geochemistry of clay minerals. Clay Min 31: 1–24
Sillitoe R (1991) Gold metallogeny of Chile. Econ Geol 86: 1187–1205
Sillitoe RH, Hedenquist JW (2003) Volcanotectonic settings, ore-fluid compositions and epithermal precious metal deposits. In: *Simmons SF, Graham I* (eds) Volcanic, geothermal, and ore-forming fluids: rulers and witnesses of processes within the earth. Soc Econ Geol Spec Publ 10: 315–343
Simmons SF, White NC, John D (2005) Geological characteristics of epithermal precious and base metal deposits. In: *Hedenquist JW*, et al (eds) Economic Geology 100th Anniversary Volumen. Soc Econ Geol, Littleton, Colorado, USA, pp 485–522
Simon G, Huang H, Penner-Hahn JE, Kesler SE, Kao LH (1999) Oxidation state of gold and arsenic in gold-bearing Arsenian pyrite. Am Mineral 84: 1071–1079
Taylor HP Jr (1974) The application of oxygen and hydrogen isotope studies to problems of hydrothermal alteration and ore deposition. Econ Geol 69: 843–883
Vennemann TW, O'Neil JR (1996) Hydrogen isotopic exchange reactions between hydrous minerals and molecular hydrogen: I. A new approach for the determination of hydrogen isotope fractionation at moderate temperatures. Geochim Cosmochim Acta 60: 2437–2451
Zheng YF (1999) Oxygen isotope fractionation in carbonate and sulfate minerals. Geochem J 33: 109–126

Author's present address: *J. Carrillo-Rosúa*, Dpto. de Didáctica de las Ciencias Experimentales, Universidad de Granada, Campus de Cartuja, 18071, Granada, Spain, e-mail: fjcarril@ugr.es